



Drag forces caused by submarine glide block or out-runner block impact on suspended (free-span) pipelines—Numerical analysis



Arash Zakeri^{a,*}, Bipul Hawlader^b

^a BP America Inc. (formerly at C-CORE), 501 Westlake Park Boulevard, Houston, TX 77079, USA

^b Memorial University of Newfoundland, St. John's, NL, Canada A1B 3X5

ARTICLE INFO

Article history:

Received 13 June 2012

Accepted 18 March 2013

Available online 20 April 2013

Keywords:

Submarine glide block

Submarine out-runner block

Impact

Pipeline

Drag force

Computational fluid dynamics (CFD)

ABSTRACT

Computational fluid dynamics (CFD) approach was employed to simulate soil–pipe interaction behavior subjected to impact load. Numerical analysis is verified with results experimentally obtained in a geotechnical centrifuge. The physical experiments in centrifuge simulated the impact of soft to firm clay blocks (4 to 8 kPa of undrained shear strengths) on two model pipes (0.19 and 0.29 m in diameter), at velocities ranging between 0.04 and 1.3 m/s in a direction normal to the pipe axis. The corresponding shear strain rates ranged from about 4 to 136 s⁻¹. In this paper, a relationship between shear stress and shear strain rate for the clay blocks is first established through re-analysis of the centrifuge experiments and then used to calibrate a CFD numerical model and to complement the physical test results. The present CFD analyses covered impact velocities up to 2 m/s and investigated different pipe diameters (6.35 to 150 mm) and clay strengths. The methodology and results of the CFD analyses are discussed and compared with the observations made from the physical experiments. The experimental results were combined with the results of the CFD analyses and a simple approach is proposed to estimate the drag force caused by a glide block or out-runner block impact on a suspended (free-span) pipeline.

© 2013 Elsevier Ltd. All rights reserved.

1. Introduction

Computational fluid dynamics (CFD) numerical methods have been successfully used to analyze multiphase and multicomponent flows and to investigate fluid–structure interaction in various settings. Zakeri et al. (2012) conducted a series of physical tests in a geotechnical centrifuge simulating a glide block or an out-runner block impacting a suspended (free-span) submarine pipeline normal to its axis and proposed a method for estimating the resulting drag force. The situations tested experimentally as described in the paper by Zakeri et al. (2012), have been analyzed using the CFD software, ANSYS CFX 13.0. Herein, the experimental data, which formed the basis of the proposed method, were re-analyzed to establish a relationship between shear stress and shear strain rate for the clay blocks. This relationship was then used to calibrate a CFD numerical model and to complement the physical test results further increasing the confidence in the proposed method. The CFD analyses investigated the influence of various gravitational fields in the centrifuge tests and covered impact velocities of up to 2.0 m/s for different pipe diameters and clay strengths. The theories and methodology used in numerical modeling of the centrifuge experiments are discussed. Findings from the CFD numerical analyses are compared to the results of the physical experiments and discussed

in the context of the proposed method. Comments are also made on the limitations of the CFD numerical model.

This paper consists of mainly three parts. The first part briefly describes the centrifuge tests results (Zakeri et al., 2012). The second part deals with strain rate effects on undrained shear strength of soil and drag force on suspended pipelines. Finally, the results of numerical analyses using CFD for 28 cases are presented.

2. Terminology and definitions

Submarine density flows are important sediment-transporting mechanisms and play a major role in the construction of deep-sea fans and deltas. Their triggering mechanisms, flow dynamics, interaction with the ambient water, depositional processes and consequences of failures have been studied by many researchers. The complexity of the flow from initiation to depositional processes associated with subaqueous density flows, combined with post-depositional consolidation and soft-sediment deformation, often make it difficult to interpret the characteristics of the flow from the sedimentary record and therefore, to appropriately create models to address engineering problems. This has led to considerable confusion of nomenclature in the literature. Mulder and Alexander (2001) provide a simple yet comprehensive and encompassing classification of sedimentary density flows based on physical flow properties and briefly discuss the likely characteristics of the deposited sediments. The authors have followed their classification

* Corresponding author. Tel.: +1 713 323 2420; fax: +1 281 366 7941.
E-mail addresses: arash.zakeri@bp.com, azakeri@mun.ca (A. Zakeri).

system with some modification in this paper. The terms adopted by the authors used in this paper and elsewhere are as follows.

- **Glide block:** an intact hydroplaning block of cohesive sediment during early stages of density flow that has not been disintegrated and/or remoulded. It still carries the strength properties of the parent sliding soil mass.
- **Out-runner block:** an intact block of cohesive sediment that has departed from the parent density flow during movement due to hydroplaning and rides freely downstream. It has not been remoulded and still carries the strength properties of the parent landslide.
- **Debris flow:** a cohesive (clay-rich) flow with a minimum sediment concentration of 50% by volume that is fully remoulded and fluidized. It can be characterized by rheological models for non-Newtonian fluids (e.g. Bingham, Herschel–Bulkley models). Its velocity profile consists of a uniform plug flow over a shear layer at the base.
- **Turbidity current:** a sandy and/or clayey sediment-transporting density flow with particle concentration of less than 50% by volume. Its flow characteristic is that of a Newtonian fluid with a density that can be lower or higher than seawater.

3. The centrifuge experiments

The experiments consist of eleven (11) physical tests conducted in a geotechnical centrifuge at a gravitational field 30 times larger than that of Earth's (i.e. N , the scaling factor, is equal to 30g's).

Fig. 1 illustrates the experimental setup and instruments. Table 1 summarizes the test results and conditions in both model and prototype terms. Details of the experiments and scaling laws considerations are described in Zakeri et al. (2012). The experiments simulated impact of approximately 4.5 m high, 6.0 m wide and 12.0 long soft to firm clay blocks on 0.19 and 0.29 m pipe diameters at a direction normal to its axis. Each clay block was made from kaolin clay consolidated to have undrained shear strengths ranging between about 4 and 8 kPa. The intact and remoulded shear strengths were measured using a T-bar during the centrifuge tests. The impact velocities (measured by a string potentiometer attached to the cart) ranged between 0.04 and 1.3 m/s. Shear strain rate was defined by:

$$\dot{\gamma} = \frac{U}{D} \quad (1)$$

where, D is the pipe diameter and U is the impact velocity of the clay block. The strain rates in the experiments ranged between 4.3 and 136.6 reciprocal seconds.

Zakeri et al. (2012) adopted a geotechnical approach to relate the impact drag force to the shear strain rate defined as Eq. (1). It was proposed that the drag force per unit length of pipeline, F_D , can be estimated from the following general form of equation.

$$F_D = k \times s_{u(ref)} \times D \quad (2)$$

where k is the model parameter (a constant or shear strain rate dependent) and $s_{u(ref)}$ is the undrained shear strength of the soil taken at the reference shear rate, $\dot{\gamma}_{ref}$. In this study, reference

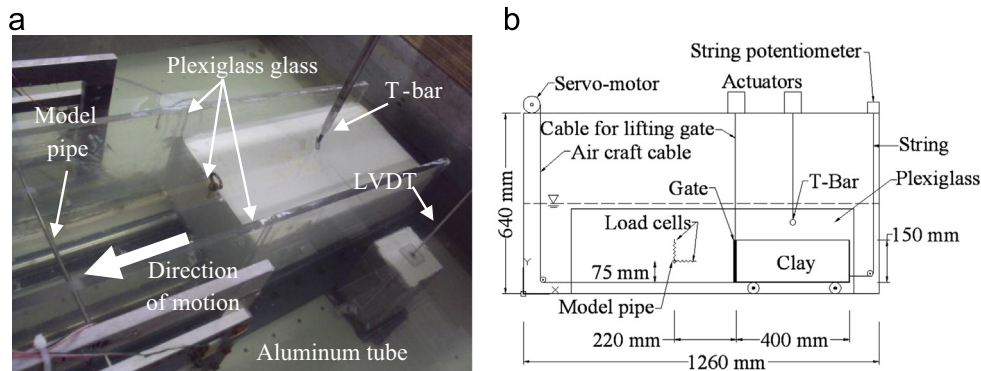


Fig. 1. Experimental setup in geotechnical centrifuge (Zakeri et al., 2012). (a) Clay block placed on the L-shaped cart ready for testing. (b) Setup elevation view with dimensions.

Table 1

Summary of the centrifuge experiments and results in model and prototype terms.

Test no.	Impact velocity (m/s)	Pipe diam.		Undrained shear strength at pipe* s_u (kPa)		Horizontal drag force per unit length, F_D		Shear strain rate (1/s)	k -Parameter
		Model (mm)	Prototype (m)	Intact	Remoulded	Model (N/m)	Prototype (kN/m)		
1	0.16	6.35	0.19	4.3	1.4	327	9.81	24.5	12.0
2	0.21	6.35	0.19	4.7	2.0	333	9.99	32.8	11.2
3	0.10	6.35	0.19	4.4	2.0	297	8.91	16.5	10.8
4	0.10	9.52	0.29	4.1**	1.4	385	11.55	10.8	9.9
5	0.20	9.52	0.29	4.1**	1.4	383	11.49	21.4	9.9
6	1.30	9.52	0.29	4.4	2.1	609	18.27	136.6	14.7
7	0.77	9.52	0.29	6.0	2.4	729	21.87	81.4	12.8
8	0.30	6.35	0.19	6.7	4.3	484	14.52	47.8	11.3
9	0.20	6.35	0.19	7.5	3.7	490	14.7	32.1	10.2
10	0.10	6.35	0.19	8.0	4.5	522	15.66	16.2	10.3
11	0.04	9.52	0.29	7.8	3.7	687	20.61	4.3	9.3

* The values reported represent average measured intact and remoulded undrained shear strengths at the vertical location immediately above and below the model pipe.

** The undrained shear strength for Tests 4 and 5 were estimated from Test 1 shear strength profile.

strain rate corresponds to the strain rate in T-bar tests, and therefore the $s_{u(ref)}$ represents the shear strength obtained from T-bar test. Fig. 2 shows the variation of k -parameter with shear strain rate in the centrifuge tests and the best fit line through the data. It was found that the k -parameter is strain rate dependent and can be described by the following power-law relationship.

$$k = 7.5 \times \dot{\gamma}^{0.12} \quad (3)$$

where, $\dot{\gamma}$ is in reciprocal seconds. The R -squared value for the fit was 0.79. Eq. (3) was proposed from experimental results.

4. Undrained shear strength dependency on strain-rate

The strain-rate dependent strength and stiffness of cohesive soils has been extensively investigated by a number of researchers (e.g. Biscontin and Pestana, 2000; Dayal and Allen, 1975; Diaz-Rodriguez et al., 2009; Lunne and Andersen, 2007). The undrained shear strength increases at a rate of 5–15% per log cycle of shear strain rate (e.g. Diaz-Rodriguez et al., 2009; Graham et al., 1983; Lunne and Andersen, 2007; Qu et al., 2010); however, this behavior was observed mainly for shear strain rates of up to about 1 min^{-1} (Qu et al., 2010). The general trend in the data can be captured by using an expression similar to Eq. (4) used by Zhu and Yin (2000) for shear rates greater than $\dot{\gamma}_{Ref}$.

$$\frac{s_{u,Corr.}}{\sigma'_o} = 0.2 + 0.1 \times \left(\frac{\sigma'_y}{\sigma'_o} \right) \log \frac{\dot{\gamma}}{\dot{\gamma}_{Ref.} = 10^{-5} \left(\frac{\sigma'_o}{h} \right)} \quad (4)$$

In the above equation, $s_{u,Corr.}$ is the rate corrected undrained shear strength, σ'_o is the effective confining vertical stress and σ'_y is the effective yield strength. The ratio, σ'_y/σ'_o , typically ranges between 0.3 and 1.96 corresponding to Over Consolidation Ratios (OCR's) of 1 and 8, respectively (Zhu and Yin, 2000). Others have used similar formulation to express strain rate dependency behavior of clay. For example, Boukpeti et al. (2012) used the following expression to describe the undrained shear strength and strain rate relationship.

$$s_{u,Corr.} = s_{u,Ref.} \left(1 + \kappa \times \log \frac{\dot{\gamma}}{\dot{\gamma}_{Ref.}} \right) \quad (5)$$

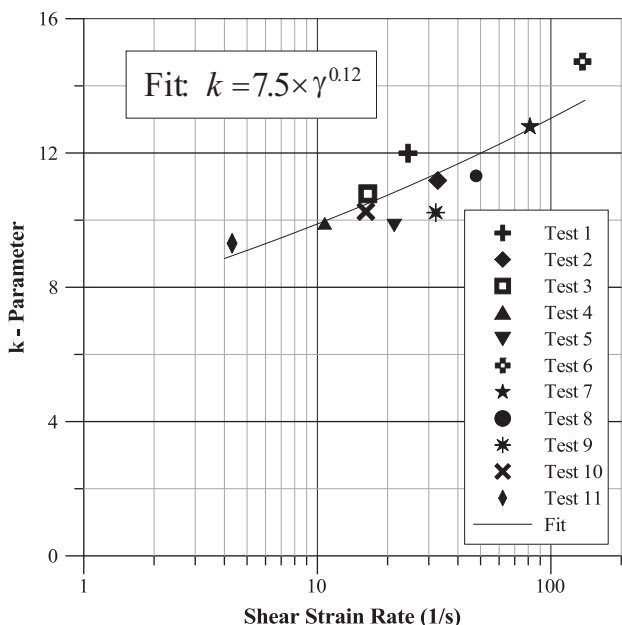


Fig. 2. Shear strain rate versus model parameter, k , in model or prototype terms (Zakeri et al., 2012).

Where, $s_{u,ref}$ is the shear strength at the reference shear strain and κ is a model parameter ranging between 0.1 and 0.2 (or 10–20% change in shear strength per log cycle) (Graham et al., 1983; Lunne and Andersen, 2007). Other has proposed the following expression as an alternative to Eq. (5) to avoid problems with the strain rate approaching zero (Einav and Randolph, 2006):

$$s_{u,Corr.} = s_{u,Ref.} \left(1 + \lambda' \text{arc sinh} \left(\frac{\dot{\gamma}}{\dot{\gamma}_{Ref.}} \right) \right) \quad (6)$$

where, $\lambda' = \kappa/\ln 10$. Eq. (6) is basically equivalent to Eq. (5), but decays rapidly for strain rates lower than $\dot{\gamma}_{Ref.}$; for strain rates below $0.1 \dot{\gamma}_{Ref.}$, a minimum strength is reached which is about 4% lower than the $s_{u,Ref.}$.

Eqs. (4) and (5) seem to capture the soil behavior well for low shear strain rates (typically, less than 1 min^{-1}) and as evident in the laboratory test results carried out by Kulhawy and Mayne (1990) presented in Fig. 3. However, deviation from a linear relationship is evident in Fig. 3 after strain rate of about 10 s^{-1} and also observed in several experimental studies (i.e. Biscontin and Pestana 2000, Sheahan et al. 1996) Note that the effects of high strain rate are the interest of the present study. Biscontin and Pestana (2000) experimented with artificial soils (72% kaolinite, 24% bentonite and 4% type C fly ash) at shear rates as high as 3000 deg./min (about 100 min^{-1} or 1.7 s^{-1}) using a vane, 55 m in diameter. They express the shear stress–shear strain relationship as a power-law by:

$$s_{u,Corr.} = s_{u,Ref.} \left(\frac{\dot{\gamma}}{\dot{\gamma}_{Ref.}} \right)^\beta \quad (7)$$

where, β is model parameter found to range between 0.05 and 0.1.

Sheahan et al. (1996) demonstrated that the undrained shear strength of saturated clays at shear strain rates higher than about 50%/h becomes insensitive to the stress history and below a certain value (i.e. the threshold strain rate) it becomes insensitive to shear strain rate. Further, they concluded that this rate dependency is complex and the threshold strain rate is a function of the stress history. Strain rates used for in-situ and laboratory testing cover an extremely wide range and may vary orders of magnitude. For example, the strain rate recommended for field vane testing (ASTM, D2573-08) is 0.1 deg/s ($\sim 0.003 \text{ s}^{-1}$), for miniature vane testing in laboratory (ASTM, D4648-10) ranges between 1 and 1.5 deg/s (~ 0.033 and 0.0533 s^{-1}), for undrained direct simple shear testing (ASTM, D6528-07) is 5%/h ($\sim 1.4 \times 10^{-5} \text{ s}^{-1}$), and for undrained triaxial compression testing (ASTM, D4767-11) is 1%/h ($2.78 \times 10^{-6} \text{ s}^{-1}$). Field T-bar and ball penetrometers are pushed in at a rate of about 1 s^{-1} (Stewart and Randolph, 1994). While all

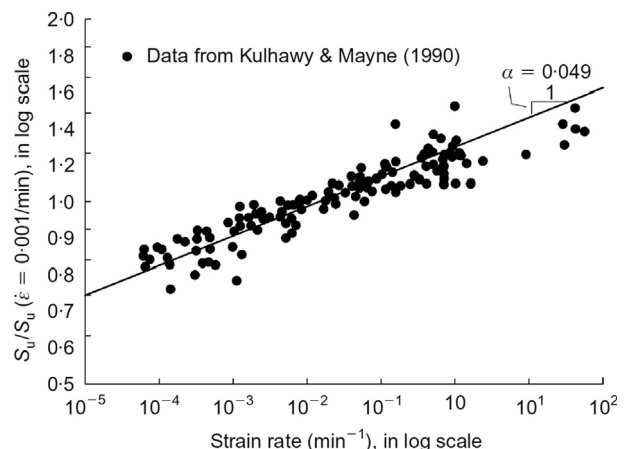


Fig. 3. Undrained shear strength against strain rate data, Kulhawy and Mayne (1990). The vertical axis is $s_{u,Corr.}$ with reference to a shear rate of $10^{-3} (1/s)$.

these tests are commonly used and perfectly accepted, one needs to apply caution when using Eqs. (5)–(7) to estimate $s_{u,Corr}$ in absence appropriate laboratory testing and knowing the value of $\dot{\gamma}_{Ref}$. For example, the rate corrected shear stress for a soil ($s_{u,Ref}=2$ kPa at $\dot{\gamma}_{Ref}=10^{-5}$ s⁻¹) sheared at a rate of 5 s⁻¹ as estimated by Eq. (7) would be about 3.8 and 7.4 kPa for β values of 0.05 and 0.1, respectively. This is an increase of about 2 folds or higher depending of the value of β selected. Choosing another value for $\dot{\gamma}_{Ref}$ would yield different results.

The shear strain rates involved in the case of debris flow and glide-block impact on pipelines is far greater than those used in the conventional field and laboratory shear strength testing. Sheahan et al. (1996) concluded that behavior of saturated clays at shear strain rates higher than 50%/h ($\sim 1.4 \times 10^{-4}$ s⁻¹) becomes insensitive to the stress history and all cohesive soils behave as viscous materials at very high strain rates. This is a key conclusion and indicating that a different approach is required to capture the rate dependency of shear strength at very high shear rates.

The Herschel and Bulkley (1926) model, expressed by Eq. (8), is a generalized model that describes the constitutive behavior of visco-plastic materials in motion. Three parameters characterize this relationship: the consistency (K), the flow index (n), and the yield shear stress (τ_c). These parameters are determined through experiments.

$$\tau = \tau_c + K \times \dot{\gamma}^n \quad (8)$$

The Herschel–Bulkley model has been widely used to describe the constitutive behavior of non-Newtonian fluids that exhibit yield stress and a non-linear response with either an increase in viscosity (shear thickening, $n > 1$), or a decrease in viscosity (shear thinning, $n < 1$) with increase in strain rate. It has successfully been applied to model the behavior of kaolinite suspensions (Wan, 1985; Zakeri et al., 2009b), muds (Coussot, 1997; Coussot and Piau, 1994) and debrites of past submarine landslides (Locat, 1997; Locat et al., 1990). Further, it has been implemented in fluid dynamics software, such as CFX (2011b), for numerical analysis and landslide run-out simulation codes such as BING (Imran et al., 2001; Marr et al., 2002). Gauer et al. (2005) provides an example where the Herschel–Bulkley model was successfully applied to back-analyze case histories of submarine debris flows.

The Herschel–Bulkley model, with $\tau_c=0$, is exactly equivalent to the soil mechanics power law model (Eq. (7)) where $K = s_{u,Ref}/\dot{\gamma}_{Ref}^\beta$ and $n=\beta$ (Boukpeti et al., 2012). With $n=1$, the Herschel–Bulkley model is reduced to what is known as the Bingham model (Bingham and Green, 1920) described by Eq. (9).

$$\tau = \tau_c + \mu_B \times \dot{\gamma} \quad (9)$$

In the Bingham model, μ_B is referred to as the dynamic Bingham viscosity (also called plastic viscosity). De Blasio et al. (2004b) provides an example where the Bingham model was successfully used to simulate the flow of natural debris flows. Other models such as the Casson (1959) and the bi-linear (Locat, 1997) have also been used to describe the shear stress–shear strain rate relationship for muds and natural soils, but they are less common. These models are expressed by:

$$\text{Casson (1959)} : \sqrt{\tau} = \sqrt{\tau_c} + \sqrt{K \times \dot{\gamma}} \quad (10)$$

$$\text{Locat (1997)} : \tau = \tau_c + \nu \times \dot{\gamma} + \left(\frac{c}{\dot{\gamma} + \dot{\gamma}_0} \right) \quad (11)$$

where, the model parameters K , ν (viscosity) and c in Eqs. (10) and (11) differ from those in Eqs. (8) and (9), and are determined empirically through viscosity tests.

The appropriateness of any shear stress–shear strain rate constitutive model for applying to a situation depends on its range of validity. Eqs. (4)–(7) have been proven to adequately describe

the shear stress–shear rate relationship for wide range of clayey soils at low shear strain rates; however, they fail to do so at shear rates few orders of magnitude higher than the reference shear rate which ranges from about 10^{-3} to 10^{-5} s⁻¹. Eqs. (4) and (5) hold when the logarithm of the shear rate is within a couple of decades greater than of the reference strain rate beyond which, the behavior is better described by Eq. (7) for shear rates of perhaps less than unity. The Herschel–Bulkley model can potentially fully describe the shear stress–shear strain rate relationship for wide range of shear rates. Further, it offers a good deal of flexibility and numerical stability when coded into hydrodynamic formulations or other shear strain rate based codes. However, it is important to correctly estimate or measure the yield stress as it would affect the calculated shear stresses at very low shear strain rates. The vane-in-cup rheometers are believed to provide the best means for determining both the yield stress and basic shear rate–shear stress characteristics for viscous shear thinning suspensions (Boger, 2006). For example, one can use the Brookfield Ultra DV-III vane-in-cup rheometer (Brookfield, 1998) to conduct both the miniature laboratory vane and viscosity testing in accordance to standards ASTM (D4648-10 and D2196-05), respectively, and to fully establish the shear stress–shear strain rate relationship for a cohesive soil.

5. CFD simulation approach and theory

ANSYS CFX 13.0 is a general purpose CFD program that includes a solver based on the finite volume (FV) method for unstructured grids, as well as pre- and post processing tools for simulation definition and data extraction, respectively. The FV method uses the integral form of the conservation equations. With tetrahedra or hexahedra Control Volumes (CVs), unstructured grids are best adapted to the FV approach for complex 3D geometries (Ferziger and Perić, 2002). In general, there are two types of multiphase flows: disperse flows and separated flows. The disperse flows consist of finite particles, such as drops or bubbles (the dispersed phase) distributed in a connected volume of another continuous phase (fluid), whereas, the separated flows comprise two or more continuous streams of different fluids separated by interfaces (Brennen, 2005). A general description of the theory and the associated differential form formulations used to analyze the centrifuge experiments are included in Appendix A.

Submarine density flows such as debris flows, glide blocks and out-runner blocks, constitute an incompressible two-phase flow regime and can be modeled using fluid dynamics constitutive equations (e.g. De Blasio et al., 2005, 2004a, 2004b; Gauer et al., 2006, 2005; Harbitz et al., 2003). CFD technique has also successfully been used to simulate flume experiments of clay-rich slurries and their impact on suspended and laid-on-seafloor pipelines (Zakeri, 2009; Zakeri et al., 2009a).

Glide blocks or out-runner blocks typically reach conditions where hydroplaning occurs which in turn, results in high velocities and long run-out distances. Upon impact on a pipeline, the soil–structure interaction takes place at high shear strain rates and fully undrained conditions. Therefore, it is essential to correctly establish the relationship between the shear stress and the shear strain rate, particularly at high shear rates, in order to estimate the impact drag force. Further, in subaqueous impact situations a volume of ambient water is entrapped behind the pipe in zone known as the “wake”. This volume of entrapped water plays a role in the magnitude of the drag force as it controls the surface area where soil interacts with the pipe. CFD technique is capable of correctly modeling both the shear stress dependency on the shear strain rate and the effect of the entrapped water on the drag force. In this approach, the buoyancy effects are considered and the drag

forces resulting from both the water and clay are calculated from the viscous and dynamic pressures exerted by each phase on the pipe.

6. CFD simulation setup

6.1. General

The experiments simulated impact of an intact block of clay on a suspended submarine pipeline at a direction normal to its axis. The CFD simulations, as described below, were designed to replicate the experimental setup, to investigate the effects of gravitational field and to complement the centrifuge test results. The homogeneous two-phase separated Eulerian–Eulerian multi-phase flow model of the CFX program was used to simulate the centrifuge experiments.

6.2. Domain and boundary conditions

Fig. 4 illustrates the domain geometry and example of the mesh used in the simulations. The domain width was 10 mm in all simulations. Various pipe diameters ranging between 6.35 and 350 mm were simulated. The mesh was refined within a 10 mm distance around the pipe. The grid spacing on pipe surface ranged from 0.5 to 5 mm with the smaller values corresponding to smaller pipe diameters. The maximum grid spacing elsewhere was 10 to 25 mm depending on the domain size. These grid spacings were selected based satisfactory performance pervious simulations (e.g. Zakeri, 2009). In addition, occasional mesh sensitivity analyses were performed on select domains by further reducing the grid spacing to evaluate the influence of the fineness of the mesh on the computation results.

Both the pipe surfaces were modeled as rough no-slip boundary condition. The inlet (i.e. where the clay block enters into the domain) for the flow was 5 times the pipe diameter in height. The outlet (i.e. where the block exits the domain) was modeled as opening boundary condition. The domain was filled with water initially. The side walls were modeled as symmetry boundary condition (i.e. plain strain condition with no shear stress induced on the fluids) and the walls elsewhere were in free-slip condition.

This reduced the computation time required to compute the fluid velocity field on those surfaces without affecting the drag on the pipe.

6.3. Material properties and modeling

The domain was set up for a two-phase (water and clay block) flow. Standard properties of water were used. Turbulence generated in the water was simulated using the $k-\epsilon$ model. Inherent in Eq. (3) is the dependency of the undrained shear strength on the rate of shear. By dividing both sides of Eq. (2) by pipe diameter, it follows that the shear stress increases at a rate proportional to Eq. (3). In the centrifuge experiments, the soil–pipe interaction is such that the clay shearing occurs under fully undrained condition. Therefore, from the simulation perspective an appropriate constitutive model was deemed to be the one that has the capability of increasing the stress tensor in a material from the yield value in accordance to the shear at which it is sheared. The CFX program provides a wide range of models for non-Newtonian fluids (CFX, 2011a). The clay block was modeled as a non-Newtonian fluid using the Herschel–Bulkley model. For incompressible Newtonian fluids, the shear stress is proportional to the rate-of-deformation tensor, \bar{D} , and is expressed by:

$$\bar{\tau} = \mu \times \bar{D} \tag{12}$$

In Eq. (12), μ is viscosity and independent of \bar{D} , which is defined by:

$$\bar{D} = \left(\frac{\partial u_j}{\partial x_i} + \frac{\partial u_i}{\partial x_j} \right) \tag{13}$$

Where, u and x are the velocity and direction vectors, respectively. For some non-Newtonian fluids (e.g. those described by Eqs. (8) and (9)), the shear stress can similarly be written in terms of a non-Newtonian dynamic viscosity, η , as follows:

$$\bar{\tau} = \eta(\bar{D}) \times \bar{D} \tag{14}$$

In general, η is a function of all three invariants of the rate-of-deformation tensor. However, in the non-Newtonian models available in ANSYS CFX, η is considered to be a function of the shear rate. It is related to the second invariant of \bar{D} , and is

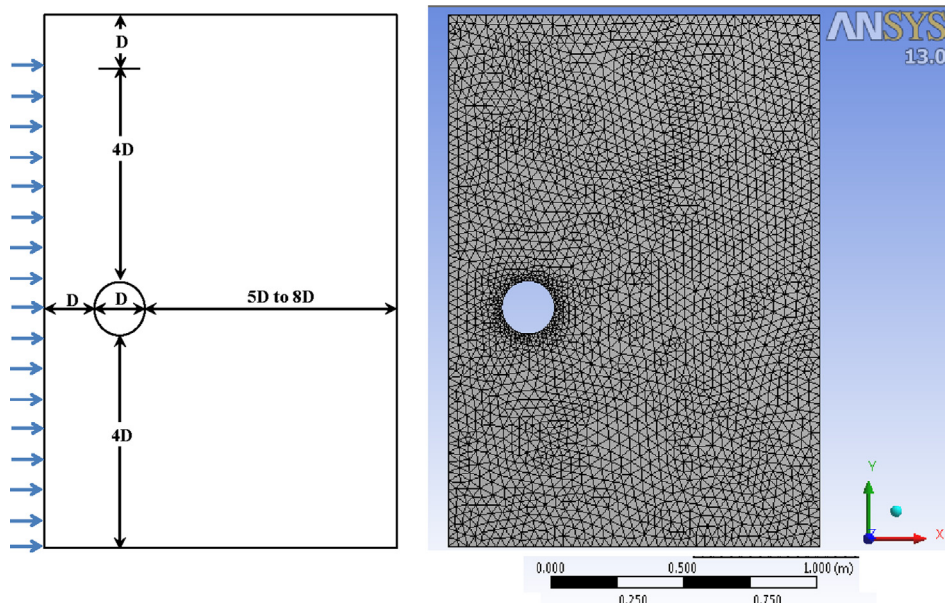


Fig. 4. Domain geometry (left) and mesh example with minimum 10,500 tetrahedron elements (right). The clay block enters the domain from the left (i.e. inlet) and leaves from the right (i.e. outlet).

expressed by:

$$\dot{\gamma} = \sqrt{\frac{1}{2}(\bar{D})} : \bar{D} \quad (15)$$

Temperature dependency of viscosity could also be considered in ANSYS CFX, discussion of which is irrelevant to this work. In the Herschel–Bulkley model, the shear stress tensor is described by:

$$\bar{\tau} = \bar{\tau}_c + \eta \times \bar{D} \quad (16)$$

where, the material remains rigid when $\bar{\tau} \leq \bar{\tau}_c$, and otherwise flows as a viscous fluid behavior of which is described by a power-law. In ANSYS CFX, the dynamic viscosity in the Herschel–Bulkley model for when the material starts to flow is described by (CFX, 2011b):

$$\eta = \frac{\tau_c}{\dot{\gamma}} + K_{Index} \times \left(\frac{\dot{\gamma}}{\dot{\gamma}_{Ref.}} \right)^{n-1} \quad (17)$$

In the above, K_{Index} is the consistency index in Pa s, which differs from the consistency K in Eq. (8). A series of simulations were carried out based on the results of centrifuge Tests 1, 7 and 8. As a starting point, the exponent 'n' in the Herschel–Bulkley model was set to 0.12 (i.e. equal to the exponent in Eq. (3)). This was considered appropriate as the drag forces in the centrifuge tests increased with shear rate (defined by Eq. (1)) following a power-law relationship with exponent of 0.12. The reference shear rate was set to 1E-3 (1/s) based on the rates at which the T-bar tests were conducted in the centrifuge experiments (corrected to prototype terms). The results of calibration simulations indicated that a value of 0.125 for the exponent with consistency index of 7.5 would provide satisfactory results.

The clay block movement was modeled as laminar free surface flow of a buoyant continuous phase. In a two-phase flow, the difference between the phase densities produces a buoyancy force reflected in the governing equations of the flow. A source term, $S_{M, Buoyancy, \alpha} = (\rho_\alpha - \rho_{ref}) \times g$, was therefore added to the momentum equations; where, g is the gravitational acceleration. The buoyancy reference density, ρ_{ref} , was set equal to the density of water, 977 kg/m³, and the pressure in the momentum equation was set with respect to the absolute pressure. The density of clay was assumed to be 1685 kg/m³ for all simulations.

6.4. Computational details

Various inlet (clay block impact) velocities and pipe diameters were simulated at different gravitational fields. At time zero, the volume fraction and velocity field of the water in the domain were set to be 1 and nil, respectively. A transient scheme was utilized to run the simulations. The time-steps were selected in consideration with the following rule:

$$\Delta t = \frac{0.3L_{Scale}}{\max(U_{BC}, U_{Node})} \quad (18)$$

where, L_{Scale} is the length scale, U_{BC} and U_{Node} are the velocities at the boundary and nodes, respectively. Here, U_{BC} was the controlling parameter. The length scale was taken as the minimum of $L_{vol} = \sqrt[3]{\text{Domain Volume}}$ and $L_{ext} = (L_x, L_y, L_z)$, or conservatively, as the mesh nodal spacing. As such, a 10 mm length scale was selected for the simulations and the corresponding time-steps ranged between 0.001 and 0.025 s depending on the inlet velocity.

CFX uses a coupled solver, which solves the transport equations for the velocity and pressure fields as a single system. This solution approach uses a fully implicit discretization of the equations at any given time. The non-linear equations are linearized and assembled into the solution matrix, which are then solved using a Multi-Grid (MG) accelerated Incomplete Lower Upper (ILU) factorization technique—it is an iterative solver (CFX, 2011b). In the simulations,

the advection term was solved using the High Resolution Scheme given by Eq. (19), in which the factor β is calculated locally to be as close as possible to 1 without violating boundedness principles.

$$\phi_{ip} = \phi_{up} + \beta \nabla \phi \times \Delta \vec{r} \quad (19)$$

In the above equation, ϕ is a variable and the subscripts 'ip' and 'up' denote the integration point in the middle of the element face and the value at the upwind node, respectively, and $\Delta \vec{r}$ is the vector from the upwind node to the integration point. Computation of the factor β is based on the Barth and Jespersen (1989) method. The transient term in the simulations was approximated by the Second Order Backward Euler scheme. A Root-Mean-Square (RMS) value of 5×10^{-5} was selected as the convergence criterion for normalized values of the equation residuals.

7. Results and discussion

Table 2 summarizes the simulation parameters and the computed results. Fig. 5 compares the k -parameters for the centrifuge experiments and those computed from the CFD simulations. The simulations performed very satisfactorily. For example, Fig. 6 presents snapshots from simulation No. 27 to illustrate the movement of the clay block in the domain and around the pipe. It also shows three snapshots of taken from Test 6 (Zakeri et al., 2012) for comparison purposes. The CFD simulations closely reproduced the observations made by the camera during the centrifuge tests. Fig. 7 presents the clay velocity and shear strain rate immediately outside pipe surface and the shear stress and total pressure (from the clay and water) exerted on the pipe surface for simulation No. 27 during the steady-state condition. The clay velocity, shear strain rate and shear stress plots shown on Fig. 7 are essentially the same for the upper and lower halves of the pipe. Therefore, the total shear stress exerted is double than what is plotted. The total pressure shown on Fig. 7 is the pressure distribution on the pipe surface. Total pressure is defined as the pressure that would exist at a point if the fluid was brought instantaneously to rest such that the dynamic energy of the flow converted to pressure without losses. In this case (clay modeled as incompressible, undrained), the total pressure is expressed by the Bernoulli's equation (Eq. (20)):

$$P_{Total} = P_{Static} + \frac{1}{2} \rho (\vec{U} \times \vec{U}) \quad (20)$$

which is the sum of the static and dynamic pressures. In Eq. (20), ρ is the clay density and U is the velocity field. The shear stress is tangential to the pipe surface and the total pressure, normal. The drag force exerted is the sum of the shear stress and the total stress over the pipe surface. The pressure force is obtained by integrating the total pressure over the pipe surface. The shear strain rate, obtained from Eq. (15), differs from Eq. (1). The shear stress, obtained from Eq. (14), presents the viscous effect. It is clear that the dynamic effects are dominant compared to those of viscous. The dominance of the inertia effects is also quite evident in Fig. 7 when comparing the wall total pressure and the wall shear plots

It should be noted that in terms of kinematics there are differences between steady flow of non-Newtonian fluids and Newtonian fluids around a cylinder. For example, the separation point for a Newtonian fluid typically occurs at about 90 degrees whereas in the case of non-Newtonian fluid of power-law and Herschel Bulkley type, the separation point is a function of the Reynolds number and the index, n . This has been demonstrated by the detailed work of Bharti et al. (2006). They studied steady flow of power-law fluids, both shear-thinning ($n < 1$) and shear-thickening ($n > 1$) around a cylinder at Reynolds numbers ranging between 5 and 40. They found that the size of recirculation zone

Table 2
Summary of simulation results.

Sim. no.	g-level (m ² /s) (g)	Impact velocity (m/s)	s _w (kPa)	Pipe diameter (m)	Drag force (N/m)	Shear rate (1/s)	k-Parameter	Remarks
1	1	0.16	4.30	0.00635	325.7	24.41	11.93	Calibration run, Test 1
2	10	0.16	4.30	0.00635	300.8	24.41	11.01	Calibration run, Test 1
3	10	0.16	4.30	0.00635	299.6	24.41	10.97	Calibration run, Test 1
4	15	0.90	5.98	0.015	1,089.0	60.00	12.14	Calibration run, Test 7
5	1	2.50	6.00	0.2	12,491.9	12.50	10.41	
6	10	1.00	6.00	0.05	3,250.5	20.00	10.84	
7	15	1.75	8.00	0.015	1,621.2	116.67	13.51	
8	10	1.30	6.73	0.01	951.9	136.55	14.86	Calibration run, Test 8
9	1	7.00	6.00	0.2	14,227.5	35.00	11.85	
10	1	1.00	5.98	0.025	1,825.6	40.00	12.21	Calibration run, Test 7
11	5	0.90	5.98	0.015	1,078.5	60.00	12.02	Calibration run, Test 7
12	15	1.30	6.73	0.01	954.2	136.55	14.89	Calibration run, Test 8
13	20	0.90	5.98	0.015	1,103.8	60.00	12.31	Calibration run, Test 7
14	20	0.45	6.00	0.015	1,035.1	30.00	11.50	
15	20	0.75	5.98	0.015	1,060.0	50.00	11.82	Calibration run, Test 7
16	20	1.40	6.00	0.015	1,142.3	93.33	12.69	
17	20	1.40	6.00	0.035	2,453.8	40.00	11.68	
18	1	9.50	6.00	0.125	10,036.0	76.00	13.38	
19	1	8.00	4.00	0.15	7,686.7	53.33	12.81	
20	1	0.50	6.00	0.035	2,052.6	14.29	9.77	
21	1	0.50	6.00	0.035	2,256.5	14.29	10.75	
22	1	6.75	6.00	0.15	10,651.5	45.00	11.84	
23	10	2.00	8.00	0.02	2,146.1	100.00	13.41	
24	10	1.25	4.00	0.01	554.1	125.00	13.85	
25	10	0.70	4.00	0.01	517.2	70.00	12.93	
26	10	1.00	8.00	0.01	1,097.0	100.00	13.71	
27	1	2.00	8.00	0.20	16,629.4	10.00	10.39	
28	1	6.75	4.50	0.15	8,270.0	45.00	12.25	

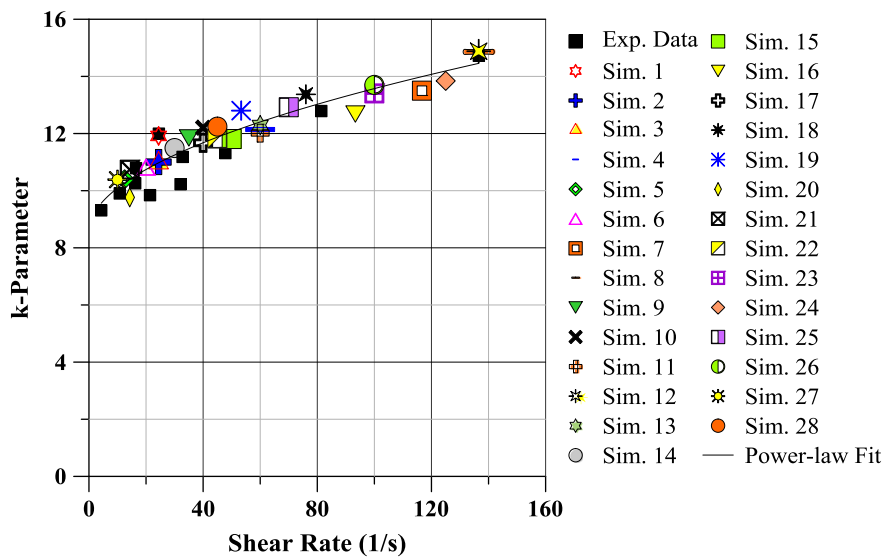


Fig. 5. k-parameter from the centrifuge experiments and CFD simulations.

and point of separation are a function of the power-law index and Reynolds number while the drag coefficient (i.e. the total drag) being insensitive to n. In terms of the behaviour, the Herschel–Bulkley fluid (the one used herein to model the clay) behaves similar to the power-law, except that it is rather solid at very low shear rates. Bharti et al. (2006) reported separation angles for shear thinning fluids with $0.6 \leq n \leq 1$ to range between about 28 and 62 degrees for Reynolds numbers of between 10 and 40. Similarly, for the impact situations simulated herein the separation point occurs at about ± 40 degrees from the stagnation point in front of the pipe (as it can be deduced from Fig. 7).

Inertia effects become significant for high velocity impact situations. Visco-plastic fluid flow around blunt objects has not extensively been studied. Oldroyd (1947) developed the visco-plastic

boundary layer theory in which he showed that a flowing yield stress material becomes rigid everywhere except in a thin layer around a blunt object. Consider a system consisting of a Herschel–Bulkley yield-stress material flowing past a cylinder. The lengths can be rendered dimensionless by the cylinder diameter, velocities by the impact velocity, stresses (pressure and shear) by $K(U/D)^n$, and timescale by D/U . Thus, the system is reduced to two dimensionless parameters; the Oldroyd or yield stress number (Od) for yield stress or plastic effects and the Reynolds number (Re) for the viscous effects. These parameters are as follows:

$$Od = \frac{\tau_c}{K(U/D)^n} \tag{21}$$

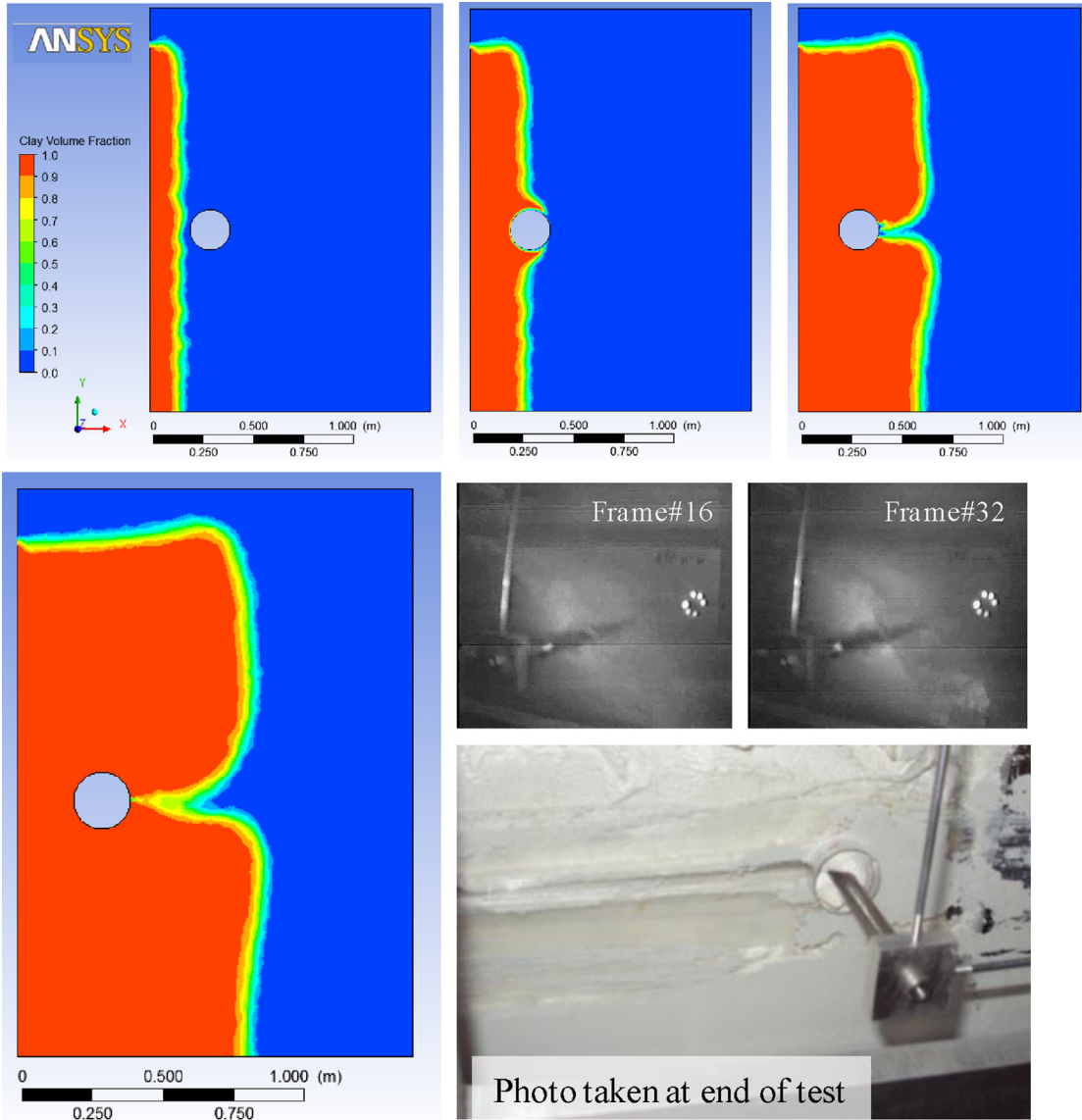


Fig. 6. Snapshots from simulation No. 27, $s_u=8.0$ kPa, impact velocity=2.0 m/s, and pipe diameter=0.2 m and centrifuge Test 6 (Zakeri et al., 2012) during and after test, $s_u=4.4$ kPa, impact velocity=1.3 m/s, and pipe diameter=0.0952 m.

$$Re = \frac{\rho \times U^2}{K(U/D)^n} \quad (22)$$

While the magnitude of the Oldroyd number is indicative of the size of the rigid zone formed in front and behind of an object (the higher the Od , the larger the zones), the Reynolds number presents the effects of inertial forces over viscous forces. Delgo De Besses et al. (2003), Tokpavi et al. (2008) and Zhu and Randolph (2011) studied the visco-plastic flow past a cylinder, but none of the studies included inertia effects. Delgo De Besses et al. (2003) and Zhu and Randolph (2011) used a Herschel-Bulkley material. Tokpavi et al. (2008) considered a Bingham fluid. Savreux et al. (2005) studied flow of a Bingham fluid normal to a flat plate and considered both the plastic and inertia effects. They noted strong dependence of the drag force to the inertia effects. All these studies were analytical and numerical.

Delgo De Besses et al. (2003) and Tokpavi et al. (2008) expressed that the drag force on the cylinder is a result of the yield stress and viscous effects. However, their study only included the yield stress effects and described the plastic drag

coefficient, C_D^* , as:

$$C_D^* = \frac{F_D}{AK(U/D)^n Od} \quad (23)$$

where, A is the projected area perpendicular to the flow direction. Savreux et al. (2005) presented the drag coefficient, C_D^* , as a function of Re and Od .

Zhu and Randolph (2011) proposed the following equation for estimating the viscous force, F_n , for a Herschel-Bulkley fluid, with strain rate effects associated directly with the flow velocity:

$$F_n = N \frac{S_{u,Ref.}}{1 + \eta} \left[1 + \eta \left(\frac{f(U/D)}{\dot{\gamma}_{Ref.}} \right)^\beta \right] A \quad (24)$$

where, N is a resistance factor (or bearing capacity factor) and η is a viscous property expressed by Eq. (25), and f is a factor that ranges between 0.8 and 1 based on the scatter in their numerical analysis results with a recommended average value of 0.88.

$$\eta = \frac{1}{Od} \left(\frac{D}{U \dot{\gamma}_{Ref.}} \right)^n \quad (25)$$

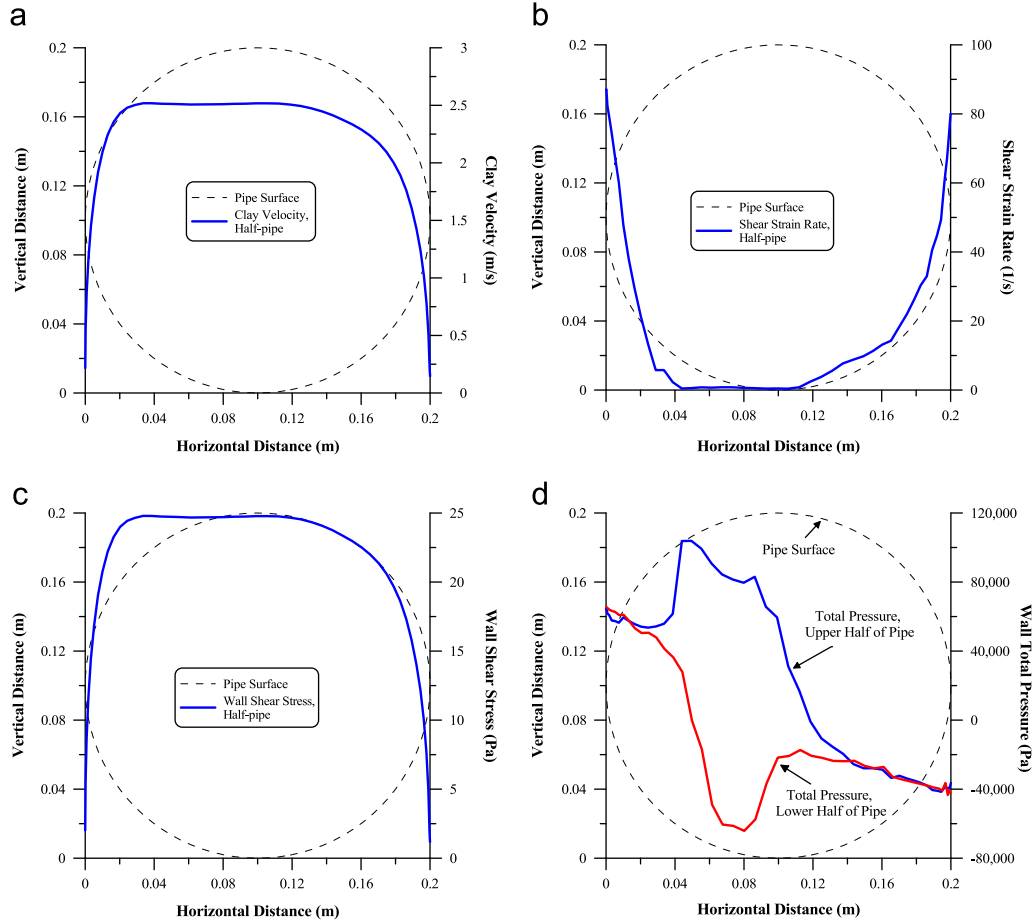


Fig. 7. CFD results at steady-state conditions, Simulation No. 27 (impact velocity = 2.0 m/s, $s_{u,0} = 8.0$ kPa): (A) clay velocity on top and bottom halves of the pipe, (B) shear strain rate on top and bottom halves of the pipe, (C) shear stress on top and bottom halves of the pipe, and (D) total pressure around pipe.

The above method (Eqs. (24) and (25)) is cumbersome for practical purposes particularly with respect to selection of appropriate values for the numerous parameters involved. Further, caution is need with respect to the reference shear strain rate. As stated earlier, all cohesive soils behave as a viscous material when sheared at rates higher than about $1.4 \times 10^{-4} \text{ s}^{-1}$ (Sheahan et al., 1996). Thus, a simpler approach seems more appropriate. To that end, the results of the centrifuge tests and numerical CFD simulations were revisited. The data were first grouped into four groups (4.0, 4.3, 6.0 and 8.0 kPa) based on the initial yield stress or the undrained shear strength determined from T-bar testing in the centrifuge. Then the total stress on the pipe was back-calculated by dividing the drag forces per unit length by the product of the pipe diameter and 7.5 (i.e. the constant in the k -parameter, Eq. (3)).

Fig. 8 presents these back-calculated shear stresses versus the shear strain rate obtained from Eq. (1) for each data. Further, it presents the Herschel–Bulkley fit through each group with the calculated model parameters and R -squared values. The shear stresses in all groups follow the same trend with a very similar Herschel–Bulkley exponent value of ranging between 0.33 and 0.4. It further shows that the Herschel–Bulkley model very well describes the shear stress exerted on the pipe.

8. Proposed approach for design purposes

A simple approach is proposed for practical and design purposes to estimate the drag force caused by glide-block and out-runner block impact on submarine pipelines. First, one needs to

determine $s_{u,Ref}$ of the collected seabed samples and establish its dependency on shear strain rate. This can be achieved through field testing and/or laboratory testing. The latter is more economic and easier to control. To achieve this a vane-in-cup rheometer capable of conducting both the miniature laboratory vane and viscosity testing in accordance to standards ASTM (D4648-10 and D2196-05), respectively, is recommended. The combination of the test sets will yield a Herschel–Bulkley model with the yield stress being the $s_{u,Ref}$ (at a reference shear strain rate standard for laboratory vane tests). It should be noted that the tests should simulate the site conditions with respect to salinity and temperature. The strain rate corrected shear stress (i.e. $s_{u,Corr}$) for the corresponding impact velocity should be obtained based on the rate dependency tests. Then the following expression can be used to estimate the drag forces per unit length normal and parallel to the pipe axis at that impact velocity:

$$\text{Normal to pipe axis : } F_{D,\perp} = N s_{u,Corr} \cdot D \sin\theta \quad (26)$$

$$\text{Parallel to pipe axis : } F_{D,\parallel} = \alpha s_{u,Corr} \cdot \pi D \cos\theta \quad (27)$$

where, α is the adhesion factor and depends on the $s_{u,Ref}$ and θ is the attack angle with respect to the pipe axis. To assess the N and α factors, one may use the guidelines provided by the American Lifeline Alliance (2001).

9. Conclusions and discussion

The CFD multiphase numerical model performed very satisfactorily in simulating the centrifuge experiments with respect to the

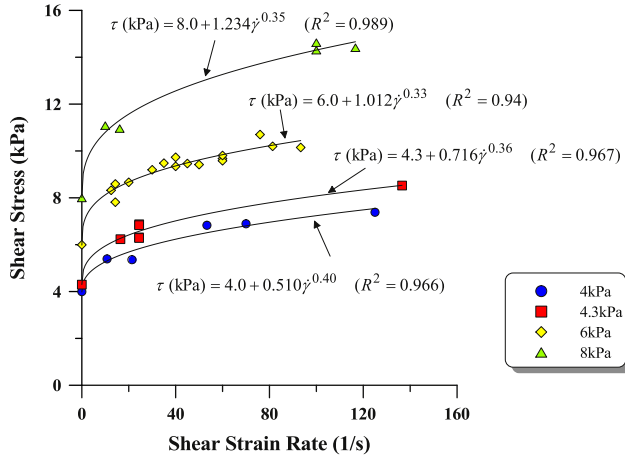


Fig. 8. Back-calculated shear stresses from results of the centrifuge tests and CFD simulations and Herschel-Bulkley model fits.

analysis of the drag forces as well as the block flow characteristics. The calculated results agreed well with those measured in the experimental program and made it possible to complement the experimental data. Such numerical analysis tools may efficiently be utilized to analyze multiphase flows of similar settings.

A major conclusion is that at high shear strain rates, the undrained shear strength of saturated clays becomes insensitive to the reference shear strain rate, $\dot{\gamma}_{Ref}$, and stress level. In other words, cohesive soils behave as viscous material when interacting with objects such as a pipeline at shear rates much larger than those used to establish the $s_{u,Ref}$ in the field or laboratory. At high shear strain rates (e.g. rapid impact of a glide block on submarine pipeline), there is insufficient time for the pore pressures to dissipate and therefore, the soil essentially behaves as a visco-plastic material along and in the vicinity of the shearing plane. Sheahan et al. (1996) also arrived at a similar conclusion from their experimental study. The magnitude of $s_{u,Ref}$ obtained from standard laboratory or field tests may slightly vary as the tests are carried out at different rates. Therefore, relationships such as those given by Eqs. (4)–(7) are helpful to compare the undrained shear strengths conventionally obtained from different testing methods with different $\dot{\gamma}_{Ref}$. These equations hold true at very low shear rates and yield reasonable estimates; however, their extrapolation to obtain $s_{u,Corr}$ at very high shear rates (i.e. orders of magnitude) requires caution, and be preferably avoided for the reasons explained earlier. It should be noted that while it is very important to correctly determine $s_{u,Ref}$, it only constitutes the starting point on the shear stress–shear strain curve encompassing shear rates in the order of 10's or even 100's reciprocal seconds, which occur in the cases of debris flow and glide block impact on pipelines and seafloor installations.

In such cases where very high shear rates exist, a more suitable approach would be to use constitutive models more suitable for describing flow of viscous material. The Herschel–Bulkley model can potentially fully describe the shear stress–shear strain rate relationship for wide range of shear rates. Further, it offers a good deal of flexibility and numerical stability when coded into hydrodynamic formulations or other shear strain rate based codes. It can easily be constituted using standard laboratory procedures as outlined in ASTM (D4648-10 and D2196-05).

Finally, the approach described herein provides a simple solution for estimating the drag forces on pipelines caused by impact of an intact block of clay. It essentially treats the cohesive soil block as a visco-plastic material, which holds true for the zones along and in the vicinity of the shearing plane. Particularly for the dynamic case of glide block impact on submarine pipeline where

the excess pore pressures constantly exist everywhere within the flowing mass as it undergoes steady deformation. As such, the method adopted here and the use of a constitutive relationship similar to the Herschel–Bulkley can describe the shear resistance of clays at particularly high shear rates and avoid the aforementioned complexities that arise from inclusion of $\dot{\gamma}_{Ref}$ to correct the shear stress.

Acknowledgements

We acknowledge the great work done by Mr. Ken Chi in conducting the physical tests that formed the basis for this paper. Mr. Chi's work was supported by C-CORE which is also appreciated by the authors. Last but not the least, we thank our reviewers for their efforts and input to our paper.

Appendix A. Multiphase incompressible fluid flow—theory and formulations

A general description of the theory and the constitutive equations used to analyze the flume experiments are briefly presented here. In the formulation, the different phases are denoted by lowercase Greek letters, α and β , and the total number of phases is N_p . In the inhomogeneous model, each phase has its own velocity and other relevant flow fields while the pressure field is shared between the incompressible fluid phases (CFX, 2011a; 2011b). In this model, the fluids interact via the inter-phase mass and momentum transfer terms. The phase continuity equation is expressed by:

$$\frac{\partial}{\partial t}(r_\alpha \rho_\alpha) + \nabla \bullet (r_\alpha \rho_\alpha \mathbf{U}_\alpha) = S_{MS\alpha} + \sum_{\beta=1}^{N_p} \Gamma_{\alpha\beta} \quad (\text{A.1})$$

where, r_α , ρ_α , and \mathbf{U}_α are the phase volume fraction, density and velocity, respectively, and $S_{MS\alpha}$ is the user specified mass sources. $\Gamma_{\alpha\beta}$ is the mass flow rate per unit volume from phase β to phase α , which must obey the rule:

$$\Gamma_{\beta\alpha} = -\Gamma_{\alpha\beta} \Rightarrow \sum_{\alpha=1}^{N_p} \Gamma_{\alpha\beta} = 0.$$

It is important to define the direction of the mass transfer in the conservative equations. A convenient method is to express $\Gamma_{\alpha\beta}$ by: $\Gamma_{\alpha\beta} = \Gamma_{\alpha\beta}^+ - \Gamma_{\beta\alpha}^+$. The term $\Gamma_{\alpha\beta}^+ > 0$ represents a positive mass flow rate per unit volume from phase β into phase α . The volume fraction is bound by: $\sum_{\alpha=1}^{N_p} r_\alpha = 1$. The momentum equation for a continuous fluid phase is expressed by:

$$\begin{aligned} \frac{\partial}{\partial t}(r_\alpha \rho_\alpha \mathbf{U}_\alpha) + \nabla \bullet (r_\alpha (\rho_\alpha \mathbf{U}_\alpha \otimes \mathbf{U}_\alpha)) = & -r_\alpha \nabla P_\alpha + \nabla \bullet (r_\alpha \mu_\alpha (\nabla \mathbf{U}_\alpha + (\nabla \mathbf{U}_\alpha)^T)) \\ & + \sum_{\beta=1}^{N_p} (\Gamma_{\alpha\beta}^+ \mathbf{U}_\beta - \Gamma_{\beta\alpha}^+ \mathbf{U}_\alpha) + S_{M\alpha} + M_\alpha \end{aligned} \quad (\text{A.2})$$

where, P_α and μ_α are the pressure and viscosity, respectively, and $S_{M\alpha}$ is the user defined momentum sources due to external body forces. M_α is the sum of interfacial forces acting on phase α due to the presence of other phases and is obtained from:

$$M_\alpha = \sum_{\beta \neq \alpha} M_{\alpha\beta} = M_{\alpha\beta}^D + M_{\alpha\beta}^L + M_{\alpha\beta}^{LUB} + M_{\alpha\beta}^{VM} + M_{\alpha\beta}^{TD} + \dots \quad (\text{A.3})$$

where, the terms indicated above, in order, represent the inter-phase drag force, lift force, wall lubrication force, virtual mass force and turbulence dispersion force. Finally, the term $(\Gamma_{\alpha\beta}^+ \mathbf{U}_\beta - \Gamma_{\beta\alpha}^+ \mathbf{U}_\alpha)$ represents the momentum transfer induced by the inter-phase mass transfer. The governing transport equations result in $4 \times N_p + 1$ equations with $5 \times N_p$ unknowns that correspond to $(u, v, w, r, P)_\alpha$ for $\alpha = 1$ to N_p . Given that the fluids in the inhomogeneous

multiphase flow share the same pressure field, the transport equations are solved by imposing the constraint of $P_\alpha = P$ for all $\alpha = 1$ to N_p .

References

- American Lifeline Alliance, 2001. Guidelines for the design of buried steel pipe. American Lifeline Alliance (ALA), American Society of Civil Engineers (ASCE).
- ASTM, D2196-05. Standard Test Methods for Rheological Properties of Non-Newtonian Materials by Rotational (Brookfield Type) Viscometer. In: A.S.f.T. Materials (Ed.), ASTM International.
- ASTM, D2573-08. Standard test method for field vane shear test in cohesive soil. In: A.S.f.T. Materials (Editor). ASTM International.
- ASTM, D4648-10. Standard test method for laboratory miniature vane shear test for saturated fine-grained clayey soils. In: A.S.f.T.M. (ASTM) (Editor). ASTM International.
- ASTM, D4767-11. Standard test method for consolidated undrained triaxial compression test for cohesive soils. In: A.S.f.T. Materials (Editor). ASTM International.
- ASTM, D6528-07. Standard test method for consolidated undrained direct simple shear testing of cohesive soils. In: A.S.f.T.M. (ASTM) (Editor). ASTM International.
- Barth, T.J., Jespersen, D.C., 1989. The design and application of upwind schemes on unstructured meshes. *Am. Inst. Aeronaut. Astronautics (AIAA)* 89, 0366.
- Bharti, R.P., Chhabra, R.P., Eswaran, V., 2006. Steady flow of power law fluids across a circular cylinder. *Can. J. Chem. Eng.* 84 (4), 406–421.
- Bingham, E.C., Green, H., 1920. Paint, a plastic material and not a viscous liquid; the measurements of its mobility and yield value. *Proc. Am. Soc. Test. Mater.* 20, 640–675.
- Biscontin, G., Pestana, J.M., 2000. Influence of Peripheral Velocity on Undrained Shear Strength and Deformability Characteristics of a Bentonite-Kaolinite Mixture, Department of Civil and Environmental Engineering, University of California, Berkeley, Geotechnical Engineering Report No UCB/GT/99-19.
- Boger, D., 2006. Rheological concepts. In: Jewell, R.J., Fourie, A.B. (Eds.), *Paste and Thickened Tailings—a Guide*, second ed. Australian Centre for Geomechanics, Nedlands, W.A, pp. 256 p.
- Boukpeti, N., White, D.J., Randolph, M., 2012. Strength of fine-grained soils at the solid–fluid transition. *Géotechnique* 62 (3), 213–226.
- Brennen, C.E., 2005. *Fundamentals of Multiphase Flow*, XXI. Cambridge University Press, Cambridge 345.
- Brookfield, 1998. Brookfield dv-iii ultra, Programmable Rheometer, Operating Instructions, Manual no. M/98-211-b0104, BROOKFIELD ENGINEERING LABORATORIES, INC., Middleboro, MA, USA.
- Casson, N., 1959. A flow equation for pigment oil suspensions of the printing ink type. In: Mill, C.C. (Ed.), *Rheology of Disperse Systems*. Pergamon Press, London, pp. 84–102.
- CFX, 2011a. Cfx Solver Modeling Guide, Cfx-Program (version 13.0) Physical Modelling Documentation. ANSYS Inc., Canonsburg, USA.
- CFX, 2011b. Cfx Solver Theory Guide, Cfx-Program (version 13.0) Theory Documentation. ANSYS Inc., Canonsburg, USA.
- Coussot, P., 1997. *Mudflow Rheology and Dynamics*, xvi. Balkema, Rotterdam 255.
- Coussot, P., Piau, J.M., 1994. On the behaviour of fine mud suspensions. *Rheol. Acta* 33 (3), 175–184.
- Dayal, U., Allen, J.H., 1975. The effect of penetration rate on the strength of remolded clay and sand samples. *Can. Geotech. J.* 12 (3), 336–348.
- De Blasio, F.V., et al., 2005. On the dynamics of subaqueous clay rich gravity mass flows—the giant storegga slide, norway. *Mar. Pet. Geol.* 22 (1–2), 179–186.
- De Blasio, F.V., Engvik, L., Harbitz, C.B., Elverhoi, A., 2004a. Hydroplaning and submarine debris flows. *J. Geophys. Res. Oceans* 109 (C1).
- De Blasio, R., et al., 2004b. Flow models of natural debris flows originating from overconsolidated clay materials. *Mar. Geol.* 213 (1–4), 439–455.
- Deglo De Besses, B., Magnin, A., Jay, P., 2003. Viscoplastic flow around a cylinder in an infinite medium. *J. Non-Newtonian Fluid Mech.* 115 (1), 27–49.
- Diaz-Rodriguez, J.A., Martinez-Vasquez, J.J., Santamarina, J.C., 2009. Strain-rate effects in mexico city soil. *J. Geotech. Geoenviron. Eng.* 135 (2), 300–305.
- Einav, I., Randolph, M., 2006. Effect of strain rate on mobilised strength and thickness of curved shear bands. *Geotechnique* 56 (7), 501–504.
- Ferziger, J.H., Perić, M., 2002. *Computational Methods for Fluid Dynamics*, XIV. Springer, Berlin 423.
- Gauer, P., Elverhoi, A., Issler, D., De Blasio, F.V., 2006. On numerical simulations of subaqueous slides: back-calculations of laboratory experiments of clay-rich slides. *Norw. J. Geol.* 86 (3), 295–300.
- Gauer, P., Kvalstad, T.J., Forsberg, C.F., Bryn, P., Berg, K., 2005. The last phase of the storegga slide: simulation of retrogressive slide dynamics and comparison with slide-scar morphology. *Mar. Pet. Geol.* 22 (1–2), 171–178.
- Graham, J., Crooks, H.A., Bell, A.L., 1983. Time effects on the stress–strain behaviour of natural soft clays. *Geotechnique* 33 (3), 327–340.
- Harbitz, C.B., et al., 2003. Hydroplaning of subaqueous debris flows and glide blocks: analytical solutions and discussion. *J. Geophys. Res. Solid Earth* 108 (B7).
- Herschel, W., Bulkley, R., 1926. Konsistenzmessungen von gummi-benzollösungen. *Colloid Polym. Sci.* 39 (4), 291–300.
- Imran, J., Harff, P., Parker, G., 2001. A numerical model of submarine debris flow with graphical user interface. *Comput. Geosci.* 27 (6), 717–729.
- Kulhawy, F.H., Mayne, P.W., 1990. *Manual on estimating soil properties for foundation design*. Palo alto, ca: Electric power research institute.
- Locat, J., 1997. Normalized rheological behaviour of fine muds and their flow properties in a pseudoplastic regime, Debris-flow hazards mitigation: Mechanics, predication and assessment, water resources engineering division. *Am. Soc. Civ. Eng. (ASCE)*, 260–269, pp.
- Locat, J., Norem, H., Schieldrop, B., 1990. Modeling the dynamics of submarine slides, Proceedings—Sixth International Congress: International Association of Engineering Geology, 4: 2849–2855.
- Lunne, T., Andersen, K.H., 2007. Soft clay shear strength parameters for deepwater geotechnical design, keynote address, Proceedings of the Sixth International Offshore Site Investigation and Geotechnics Conference: Confronting New Challenges and Sharing Knowledge, London, UK.
- Marr, J.G., Elverhoi, A., Harbitz, C., Imran, J., Harff, P., 2002. Numerical simulation of mud-rich subaqueous debris flows on the glacially active margins of the svalbard-barents sea. *Mar. Geol.* 188 (3–4), 351–364.
- Mulder, T., Alexander, J., 2001. The physical character of subaqueous sedimentary density flows and their deposits. *Sedimentology* 48 (2), 269–299.
- Oldroyd, J.G., 1947. 2-dimensional plastic flow of a bingham solid—a plastic boundary-layer theory for slow motion. *Proc. Cambridge Philos. Soc.* 43 (3), 383–395.
- Qu, G., Hinchberger, S.D., Lo, K.Y., 2010. Evaluation of the viscous behaviour of clay using generalised overstress viscoplastic theory. *Geotechnique* 60 (10), 777–789.
- Savreux, F., Jay, P., Magnin, A., 2005. Flow normal to a flat plate of a viscoplastic fluid with inertia effects. *AIChE J.* 51 (3), 750–758.
- Sheahan, T.C., Ladd, C.C., Germaine, J.T., 1996. Rate-dependent undrained shear behavior of saturated clay. *J. Geotech. Eng.* 122, 99–108.
- Stewart, D.P., Randolph, M.F., 1994. T-bar penetration testing in soft clay. *J. Geotech. Eng., ASCE* 120 (12), 6.
- Tokpavi, D.L., Magnin, A., Jay, P., 2008. Very slow flow of bingham viscoplastic fluid around a circular cylinder. *J. Non-Newtonian Fluid Mech.* 154 (1), 65–76.
- Wan, Z., 1985. Bed material movement in hyperconcentrated flow. *J. Hydraul. Eng.* 111 (6), 987–1002.
- Zakeri, A., 2009. Submarine debris flow impact on suspended (free-span) pipelines: noraml and longitudinal drag forces. *Ocean Eng.* 36, 10.
- Zakeri, A., Hawlader, B., Chi, K., 2012. Drag forces caused by submarine glide block or out-runner block impact on suspended (free-span) pipelines. *Ocean Eng.* 47, 50–57.
- Zakeri, A., Høeg, K., Nadim, F., 2009a. Submarine debris flow impact on pipelines—Part II: Numerical analysis. *Coastal Eng.* 56, 1–10.
- Zakeri, A., Si, G., Marr, J.D.G., Hoeg, K., 2009b. Experimental Investigation of Subaqueous Clay-Rich Flows, Generated Turbidity and Sediment Deposition. *Submarine Mass Movements and Their Consequences*, Austin, Texas, USA, pp. 95–106.
- Zhu, H., Randolph, M.F., 2011. Numerical analysis of a cylinder moving through rate-dependent undrained soil. *Ocean Eng.* 38 (7), 943–953.
- Zhu, J.-G., Yin, J.-H., 2000. Strain-rate-dependent stress–strain behavior of overconsolidated hong kong marine clay. *Can. Geotech. J.* 37 (6), 1272–1282.